GEOPHYSICS, VOL. 68, NO. 6 (NOVEMBER-DECEMBER 2003); P. 1877–1887, 13 FIGS., 2 TABLES.
10.1190/1.1635040

Detecting metal objects in magnetic environments using a broadband electromagnetic method

Haoping Huang* and I. J. Won*

ABSTRACT

We analyze the use of the broadband electromagnetic (EM) method in detecting metallic objects, such as unexploded ordnance (UXO), buried in magnetic environments. Magnetic rocks close to the sensor often contribute a larger in-phase response than does the target at depth, making target detection and identification difficult. On the other hand, magnetic rocks contribute little quadrature response, which gives rise to the concept of using quadrature response and apparent conductivity to detect metallic objects in highly magnetic environments.

To test this concept, we employed numeric models, physical experiments, and field studies. A layered half-space simulated conductive overburden and magnetic basement. Sphere models are used for isolated magnetic rocks and metal targets. The responses of the layered earth, magnetic rocks, and metal objects were added to obtain the approximate total response. We then inverted the EM data into apparent magnetic permeability and conductivity. The EM response at the lowest frequency was used initially to estimate apparent magnetic permeability, which let us calculate the apparent conductivity using the EM data at all frequencies. The simulations and field examples show that broadband EM sensors can detect small metal targets in magnetic environments, mainly by the quadrature component of the responses and the apparent conductivity.

INTRODUCTION

New broadband electromagnetic induction (EMI) sensors have been used increasingly at environmental sites to detect small metallic targets such as buried unexploded ordnance (UXO) and landmines. The GEM-2 and GEM-3 are examples of such sensors (Won et al., 1996, 1997, 1998). In a frequency-domain operation, these sensors measure the in-phase or quadrature responses, which may be converted to apparent conductivity using techniques described by Won et al. (1997). However, the EMI response can be severely affected by magnetic geology (e.g., mafic rocks), making target detection difficult and adding errors in the apparent conductivity. This problem has become serious when detecting UXO buried in magnetic geology such as in the Hawaiian Islands and central California, places where the U.S. government is involved in large-scale UXO cleanup projects.

Many authors have discussed the magnetic effect on electromagnetic (EM) data, as reviewed by Huang and Fraser (1998, 2000). Magnetic permeability has much less impact on the quadrature component than on the in-phase component. This gives rise to the concept of using quadrature response and apparent conductivity to detect the target in magnetic environments. The magnetic permeability can be estimated by inverting low-frequency EM data, using either in-phase static shift or the in-phase and quadrature components (Huang and Won, 2000).

This paper describes how to detect small metallic objects in magnetic environments based on quadrature response and apparent conductivity. Our theoretical study uses a magnetic and conductive half-space to simulate the magnetic geology, and spheres to simulate isolated magnetic rocks and metallic objects. Then, we show controlled experiments to verify the results and actual field data obtained in magnetic environments.

EMI RESPONSE OF A SPHERE IN A HALF-SPACE

The EM response of a layered half-space earth for a finite-source excitation is given by Ward and Hohmann (1988), among many others. If the transmitting coil excited by current $\hat{I}$ is at a height h above a half-space, the secondary magnetic field H_s at the center of transmitter coil is

$$H_s = \frac{a\hat{I}}{2}\int_0^\infty R(\lambda)\lambda \exp(-2\lambda h) J_1(\lambda a) d\lambda, \qquad (1)$$

where a is the radius of transmitter coil and J_1 the Bessel function of the first kind of order one. The term $R(\lambda)$ can be

Manuscript received by the Editor August 19, 2000; revised manuscript received April 2, 2003.
*Geophex, Ltd., 605 Mercury St., Raleigh, North Carolina 27603-2343. Email: huang@geophex.com; ijwon@geophex.com.

written as

$$R(\lambda) = \frac{Y_1 - Y_0}{Y_1 + Y_0}, \tag{2}$$

where $Y_0 = u_0 / i\omega\mu_0$ is the intrinsic admittance of free space, Y_1 is the surface admittance, i is the imaginary number, and ω is the angular frequency. For an L-layer earth, Y_1 can be obtained by the following recurrence relation

$$Y_l = \hat{Y}_l \frac{Y_{l+1} + \hat{Y}_l \tanh(u_l t_l)}{\hat{Y}_l + Y_{l+1} \tanh(u_l t_l)}, \quad l = 1, 2, \ldots, L-1, \tag{3}$$

where

$$\hat{Y}_l = \frac{u_l}{i\omega\mu_0\mu_l},$$

$$u_l = \left(\lambda^2 + k_l^2\right)^{1/2},$$

and

$$k_l = (i\omega\sigma_l\mu_0\mu_l)^{1/2}.$$

Here, t_l is the thickness, μ_l is the relative magnetic permeability, μ_0 is the magnetic permeability of free space, and σ_l is the conductivity of lth layer. At the bottom of the electrical section, we have $Y_L = \hat{Y}_L$; Y_1 is a complex function of an integral variable λ, the angular frequency $\omega = 2\pi f$, f is the frequency, the magnetic permeability μ, the conductivity σ, and the thickness t of the layers. For a given model, Y_1 can be calculated by using the recurrence relationship in equation (3). Then, Y_1 can be substituted into equation (2) and then into equation (1) to yield the responses of the sensor over the model.

The EM responses of a sphere are given by Wait (1951, 1953, 1959, 1960) and Grant and West (1965). The secondary field H^{sz} at the receiver can be written as

$$H^{sz} = (H_{r,r} + H_{\theta,r})\cos\theta_r - (H_{r,\theta} + H_{\theta,\theta})\sin\theta_r, \tag{4}$$

where $H_{r,r}$ and $H_{r,\theta}$ are radial and transverse components of the secondary field from a radial dipole source, and $H_{\theta,r}$ and $H_{\theta,\theta}$ are radial and transverse components of the secondary

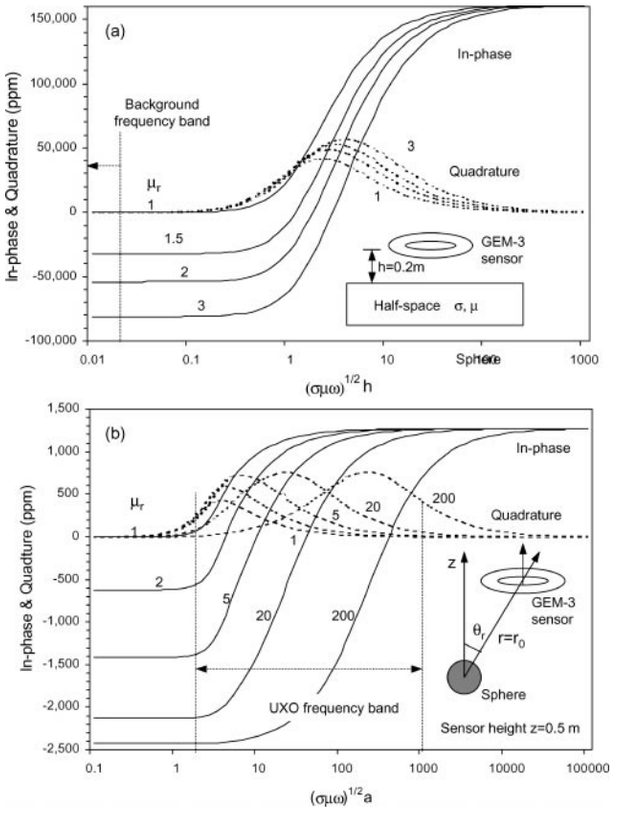

FIG. 1. In-phase I (solid curves) and quadrature Q (dotted curves) components of the response of a homogeneous half-space plotted as (a) a function of $(\sigma\mu\omega)^{1/2}h$ for various values of the relative magnetic permeability μ_r, and (b) as a function of $(\sigma\mu\omega)^{1/2}a$ for the sphere response.

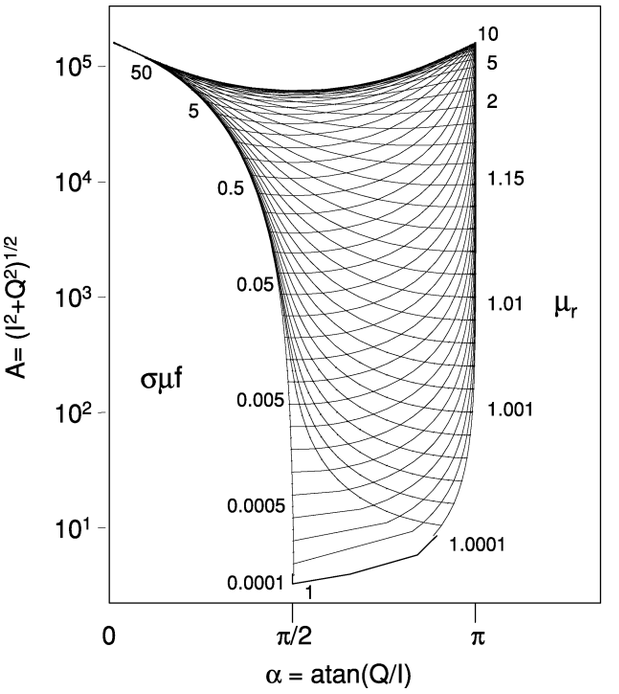

FIG. 2. Phase angle α and amplitude A for a half-space for several values of $\sigma\mu f$ and relative magnetic permeability μ_r.

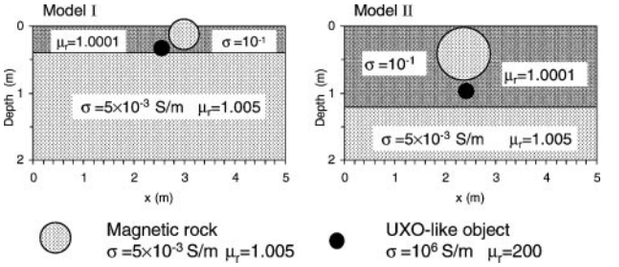

FIG. 3. Metallic targets in magnetic environments. An overburden having a conductivity 0.1 S/m (10 ohm-m) and magnetic permeability 1.0001 is above the basement having a conductivity of 5×10^{-3} S/m (200 ohm-m) and a relative magnetic permeability of 1.005. The resistive and permeable spheres simulate isolated magnetic rocks. The conductive and permeable sphere has a 0.1-m radius, a conductivity of 1×10^6 S/m, and a relative permeability of 200.

field from a transverse dipole source. Grant and West (1965) show the following expressions:

$$H_{r,r} = -\frac{m_r}{4\pi}\sum_{n=1}^{\infty}(X_n + iY_n)\frac{a^{2n+1}}{(rr_0)^{n+2}}n(n+1)P_n(\cos\theta), \tag{5}$$

$$H_{r,\theta} = -\frac{m_r}{4\pi}\sum_{n=1}^{\infty}(X_n + iY_n)\frac{a^{2n+1}}{(rr_0)^{n+2}}nP_n^1(\cos\theta), \tag{6}$$

$$H_{\theta,r} = \frac{m_\theta}{4\pi}\sum_{n=1}^{\infty}(X_n + iY_n)\frac{a^{2n+1}}{(rr_0)^{n+2}}nP_n(\cos\theta), \tag{7}$$

and

$$H_{\theta,\theta} = -\frac{m_\theta}{4\pi}\sum_{n=1}^{\infty}(X_n + iY_n)\frac{a^{2n+1}}{(rr_0)^{n+2}} \times\left[n^2P_n(\cos\theta) - \frac{n}{n+1}\cot(\theta)P_n^1(\cos\theta)\right], \tag{8}$$

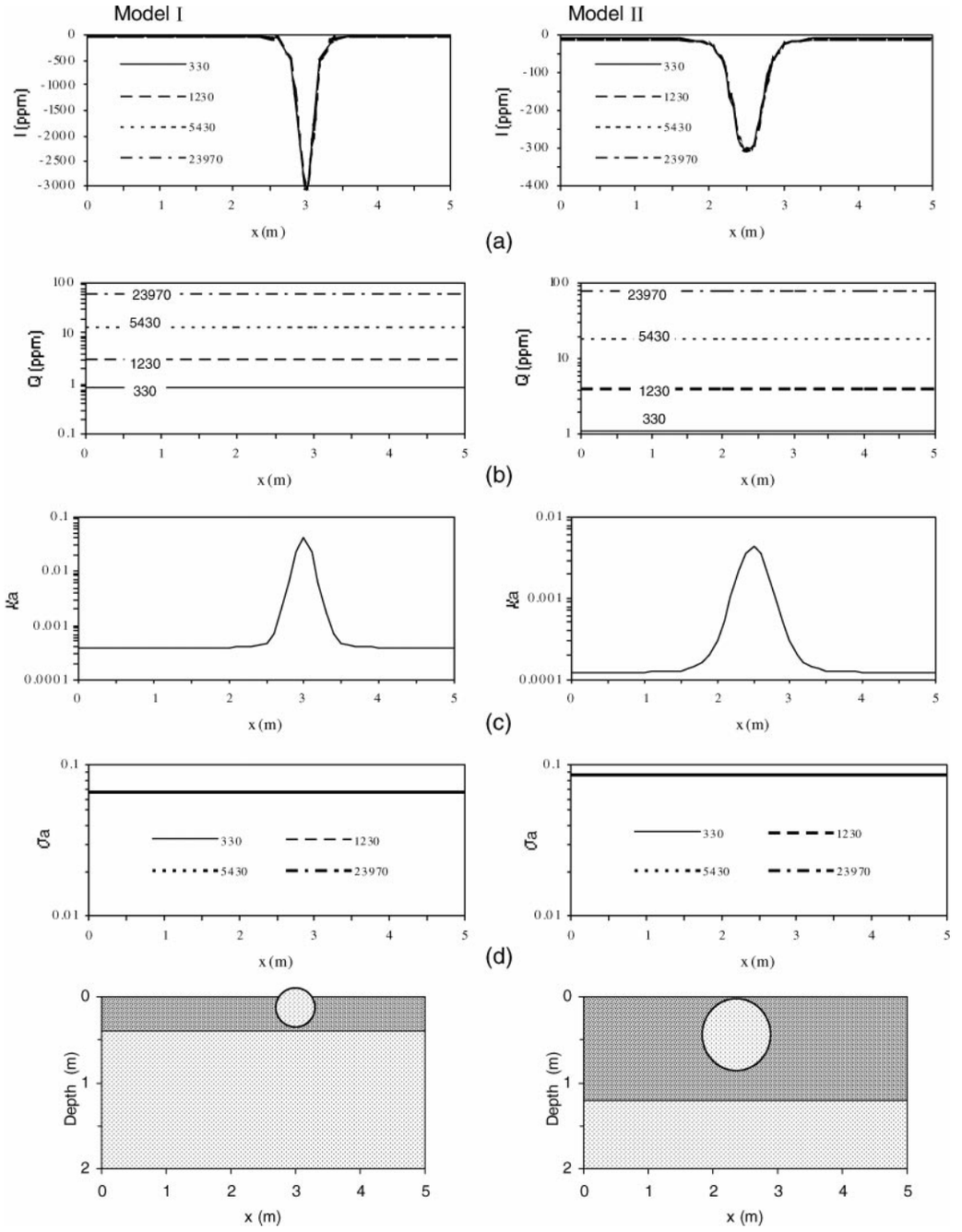

FIG. 4. Numerical modeling results. (a) In-phase and (b) quadrature profiles at 330, 1230, 5430, and 23 970 Hz over a magnetic and conductive geologic profile, along with (c) computed apparent magnetic susceptibility and (d) conductivity profiles.

where P_n is the nth order Legendre polynomial and P_n^1 is the associated Legendre polynomial. The expression $(X_n + iY_n)$, called the response function, contains all EM properties and the size of the sphere. The remaining terms are real and are governed only by the relative geometry between the sphere and the sensor locations. The real part of the response function X_n generates the in-phase response, and the imaginary part Y_n generates the quadrature response of the sphere. For a solid, conductive, and permeable sphere, the response function can be shown as

$$X_n + iY_n = \frac{\left[\frac{1}{2} - \mu_r(n+1)\right] I_{n+1/2}(ka) + kaI'_{n+1/2}(ka)}{\left(\frac{1}{2} + n\mu_r\right) I_{n+1/2}(ka) + kaI'_{n+1/2}(ka)}, \tag{9}$$

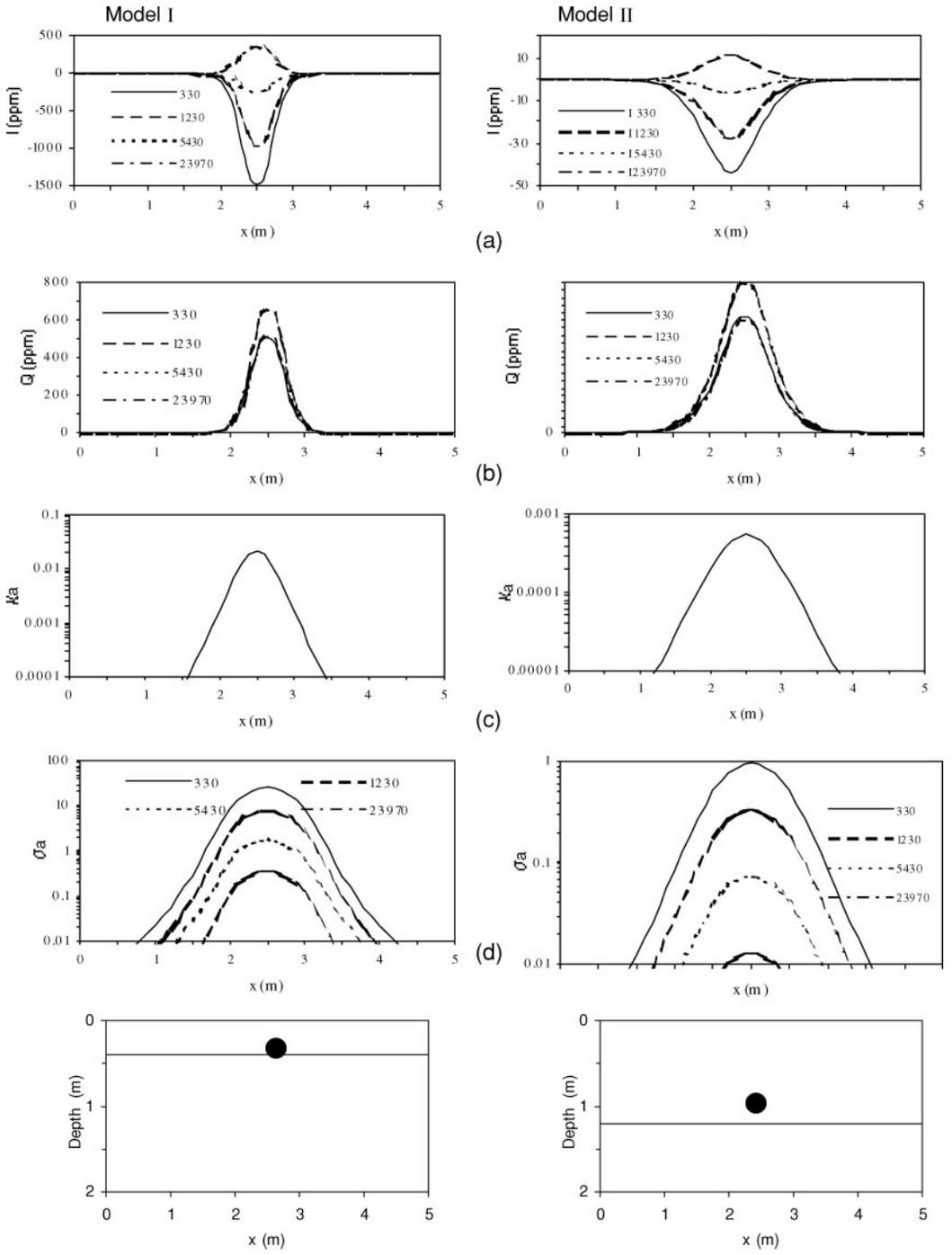

FIG. 5. The same as Figure 4, except that the model includes only metallic objects.

in which $k^2 = i\omega\mu\sigma$ and $I_{n+1/2}(ka)$ is the modified spherical Bessel function of the first kind.

Equations (1) and (4) are used to compute the in-phase (I) and quadrature (Q) responses, expressed in units of parts per million, of the primary field at the receiving coil. Figure 1 shows the I and Q responses of the normalized secondary field as functions of induction number $(\sigma\mu\omega)^{1/2}h$ over a homogeneous half-space (Figure 1a) and of $(\sigma\mu\omega)^{1/2}a$ over a sphere model (Figure 1b) for various values of μ_r. The effect of a magnetic permeability $\mu_r > 1$ is similar for the two models. First, the permeability scales up the x-axis. Second, at the low end of the x-axis, the response becomes dominated by the magnetization effect, which is in phase with, and in the same direction as, the primary field. This is the induced magnetization that occurs for an alternating magnetic field, as it does for the static earth field. At a low value of induction number [e.g., $(\sigma\mu\omega)^{1/2}h < 0.02$ in

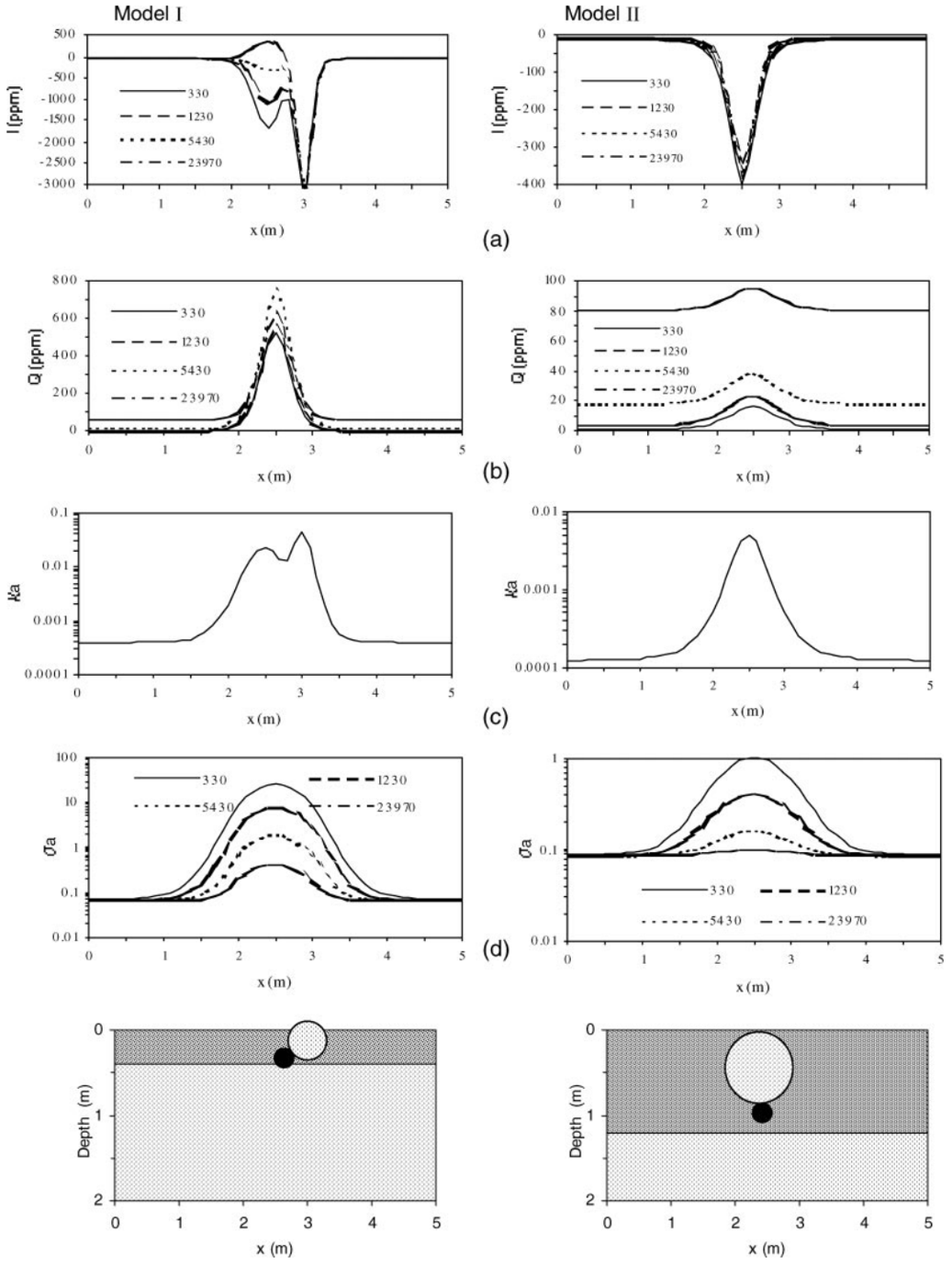

FIG. 6. The same as Figure 4, except that the model now includes both metallic objects and magnetic geology.

Figure 1a and $(\sigma\mu\omega)^{1/2}a < 1.5$ in Figure 1b], I becomes constant and Q approaches zero. For a large induction number, however, the conductive response dominates the response. For middle induction numbers, the response is a mixture of the magnetic and conductive effects.

APPARENT PERMEABILITY AND CONDUCTIVITY

Traditionally, EM data are converted to and displayed as apparent resistivity or conductivity using a homogeneous half-space model. The term apparent resistivity has been used for 80 years (Spies and Eggers, 1986). Apparent conductivity is a parameter that, in general, is related to target electrical properties and has units of conductivity.

Apparent conductivity presentation is a normalization of the EM data, which may facilitate interpretation (Spies, 1978). If the earth were truly homogeneous, the apparent conductivity would be equal to the true earth conductivity at all frequencies. In practice, the apparent conductivities are more representative of the conductivity structure than EM data (Fitterman and Stewart, 1986). For example, quadrature is proportional to conductivity in low to mid induction numbers but is inversely proportional at mid to high induction numbers as shown in Figure 1 (Grant and West, 1965; Huang and Fraser, 1998).

The raw EM data contain unwanted geologic information such as thickness variations in the conductive overburden and near-surface magnetic rocks, which can mask target anomalies. Apparent conductivity presentations generally suppress geologic noise and enhance conductive anomalies (e.g., Fraser, 1978; Spies, 1978), as will be demonstrated. If a conductive target is small or deeply buried, its response is weak and easily missed but its apparent conductivity may be high enough to be noticed.

Huang and Won (2000) describe a transformation of EM data into apparent conductivity and apparent permeability for a sensor with a finite coil separation (bistatic). The basic theory and method are the same for concentric (monostatic) sensors. Figure 2 illustrates how to convert the EM data into apparent relative permeability μ_{ra} and apparent conductivity σ_a. Amplitude $A = (I^2 + Q^2)^{1/2}$ and phase $\alpha = \text{atan}(Q/I)$ calculated from the measured I and Q locate a spot on Figure 2, from which μ_r and $\sigma\mu f$ can be determined by interpolating between the curves. Finally, σ may be obtained from the product $\sigma\mu f$ for given μ and f. Apparent magnetic permeability can be also calculated using a simple equation derived from equation (1) at resistive limit, i.e., $\omega\sigma \to 0$ (Huang et al., 2003).

In practice, based on Figure 2, we create a lookup table consisted of two logarithmic arrays: amplitude $\mathbf{A}$ $(A_1, A_2, \ldots, A_m)$ ranging from 5 to 2×10^5 ppm and phase $\alpha(\alpha_1, \alpha_2, \ldots, \alpha_n)$ from 0 to π. Each pair of A_i and α_j are associated with a pair of $(f\mu_0\mu_r\sigma)_{ij}$ and $(\mu_r)_{ij}$, resulting in two $m \times n$ tables. Given A and α, one can obtain $f\mu_0(\sigma\mu_r)$ and μ_r by using a 2D interpolation program.

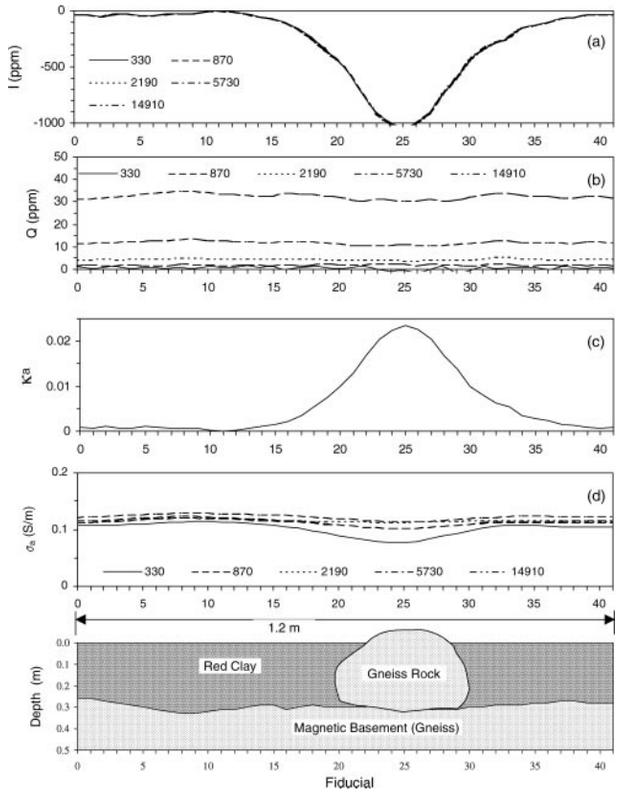

FIG. 7. (a) In-phase and (b) quadrature profiles at 330, 870, 2190, 5730, and 14 910 Hz observed over a magnetic rock and background geology as shown at bottom, (c) computed apparent magnetic susceptibility, and (d) conductivity profiles.

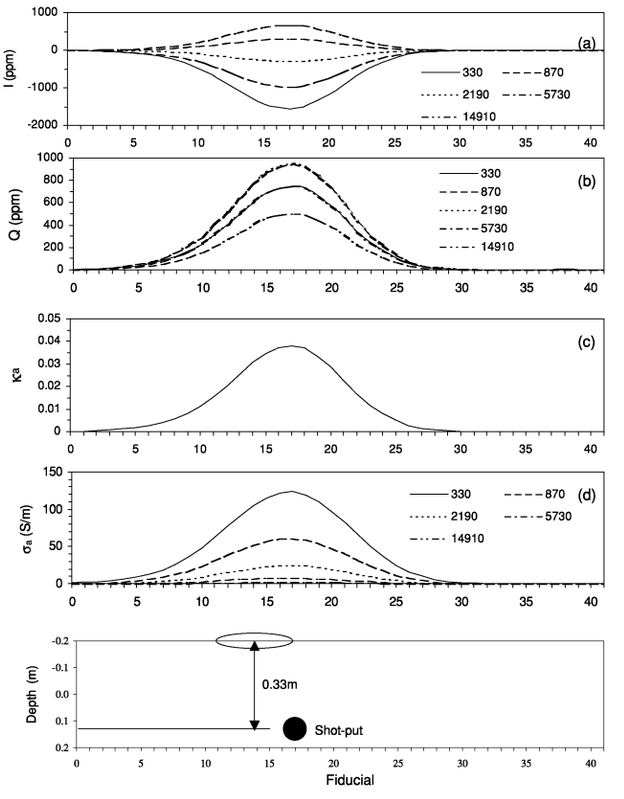

FIG. 8. (a) In-phase and (b) quadrature profiles at 330, 870, 2190, 5730, and 14 910 Hz measured over a shotput placed in air as shown at bottom, (c) computed apparent magnetic susceptibility, and (d) conductivity profiles.

APPROXIMATE NUMERICAL SIMULATION

Let us assume that metallic objects, such as UXO, are buried in a magnetic and conductive geology. We use a layered half-space to simulate the geology and spheres to simulate isolated magnetic rocks and metal targets. The EM responses for the geology and the metal objects are computed separately and then added. This approach ignores both inductive coupling and current channeling effects between the host and target, which is justified because conductivity of metal is much higher than that of soil.

Two models are shown in Figure 3. The soil layer has a conductivity of 0.1 S/m (10 ohm-m), magnetic permeability of 1.0001 (SI), basement conductivity of $\sigma = 5 \times 10^{-3}$ S/m (200 ohm-m), and permeability of $\mu_r = 1.005$, typical for mafic rocks. Inserted into each model is a magnetic boulder having the same conductivity and permeability as those of the basement, as well as a ferrous sphere having $\sigma = 10^6$ S/m and $\mu_r = 200$. Table 1 lists the position and size of the sphere used in the modeling.

We expect from Figure 1 that a metal object will produce a significant EM anomaly in both in-phase and quadrature over a broad bandwidth (30 to 24 kHz for the GEM-3), while the magnetic rocks will produce only an in-phase response. From Figure 1, we note that the magnetic geology in this case would generate predominantly in-phase responses because the induction numbers $<< 0.1$ at the highest frequency of 24 kHz. For metal objects like UXO, however, we have $2 < (\sigma\mu\omega)^{1/2}a <$ thousands generating large I and Q responses (Figure 1b). Therefore, the magnetic basement and boulders will manifest large I but negligible Q. Thus, one can detect

Table 1. Sphere model's position *x*,*z* and radius *a*, where *z* is the depth from the sensor to the center of the sphere. Bold values in columns are for the spheres simulating UXO objects.

Model	*x* (m)	*a* (m)	*z* (m)
I	**2.5**	**0.1**	**0.6**
	3.0	0.2	0.2
II	**2.5**	**0.1**	**0.9**
	2.5	0.3	0.5

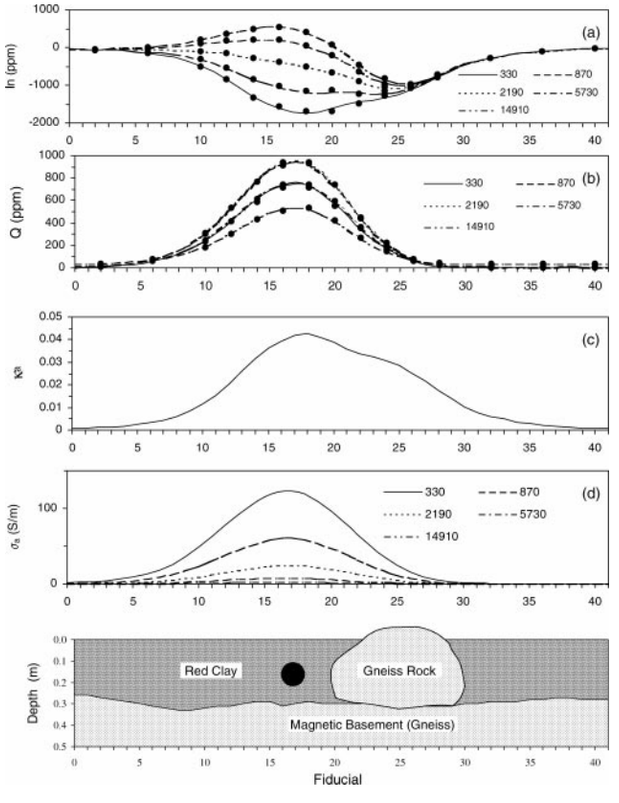

FIG. 9. (a) In-phase and (b) quadrature profiles at 330, 870, 2190, 5730, and 14 910 Hz measured over a magnetic rock, shotput, and geology background as shown at bottom, (c) computed apparent magnetic susceptibility, and (d) conductivity profiles.

Table 2. Target description for Geophex UXO test site in Raleigh, North Carolina.

Target ID	Description	*x* (m)	*y* (m)	*z* (cm)
L1	6.1"-OD×20" steel pipe, horizontal, E-W	7.25	7.25	100
L2	6.1"-OD×20" steel pipe, 45°, SW(up)-NE	2.75	2.75	110
M1	3.1"-OD×18" steel pipe, vertical	5.00	5.00	70
M2	3.1"-OD×18" steel pipe, 45°, NW(up)-SE	8.25	4.75	80
M3	2.5"-OD×12" steel pipe, horizontal E-W	8.75	1.25	50
M4	2.5"-OD×12" steel pipe, 45°, W(up)-E	5.25	1.75	60
M5	3.1"-OD×18" steel pipe, horizontal, N-S	1.75	5.25	70
M6	2.5"-OD×12" aluminum pipe, horizontal, SW-NE	1.25	8.75	50
M7	2.5"-OD×12" steel pipe, horizontal N-S	4.75	8.25	60
S1	0.8"-OD×4" steel pipe, horizontal, N-S	3.00	9.25	10
S2	0.9"-OD×6" aluminum pipe, 45°, NW(up)-SE	2.75	8.25	15
S3	1.6"-OD×6" steel pipe, vertical	2.25	7.25	30
S4	1.6"-OD×4" steel pipe, horizontal, N-S	0.75	7.00	30
S5	1.6"-OD×6" steel pipe, 45°, SW(up)-NE	3.25	6.25	30
S6	1.6"-OD×6" steel pipe, horizontal, E-W	6.75	3.75	30
S7	1.6"-OD×4" steel pipe, horizontal, E-W	9.25	3.00	30
S8	1.6"-OD×6" steel pipe, 45°, SW(up)-NE	7.75	2.75	20
S9	0.9"-OD×6" aluminum pipe, horizontal, E-W	7.25	1.75	15
S10	0.8"-OD×4" steel pipe, horizontal, E-W	7.00	0.75	10
S11	0.9"-OD×6" copper pipe, 45°, NW(up)-SE	0.75	0.75	20
S12	0.9"-OD×6" copper pipe, horizontal, N-S	9.25	9.25	15
R1	30×30(top)×33 cm (deep) diabase boulder; top at 15 cm	0.50	4.00	27

metal targets using the Q components. Alternately, metals will show high apparent conductivity since the geology itself is, by comparison, a nonconductor.

We first analyze I, Q, σ_a, and μ_r for the background geology alone. Figures 4a and 4b show the GEM-3 responses at four frequencies (330, 1230, 5430, and 23970 Hz) computed at 10-cm intervals and a sensor height of 20 cm. As expected, the in-phase responses are negative and frequency independent (the curves for all frequencies lie on top of each other), indicating that the background is magnetic but not conductive. Magnetic boulders produce sharp negative I anomalies but negligible Q. The quadrature Q is mainly produced by the soil layer. Note that the small outcropping magnetic rock produces a stronger in-phase response than does a large magnetic rock buried in soil.

Figures 4c and 4d illustrate the apparent susceptibility ($\kappa_a = \mu_{ra} - 1$) and conductivity, converted from the EM data in Figures 4a and 4b: μ_{ra} was first determined from the 330-Hz response based on Figure 2. In this case, all I data yield the same μ_{ra} because I is frequency independent, as shown in Figure 4a. The computed μ_{ra} is then used to obtain σ_a from Figure 2. The susceptibility profile reflects background geology and the magnetic rock, while the conductivity profile reflects mainly the soil layer. The apparent conductivity is virtually identical for

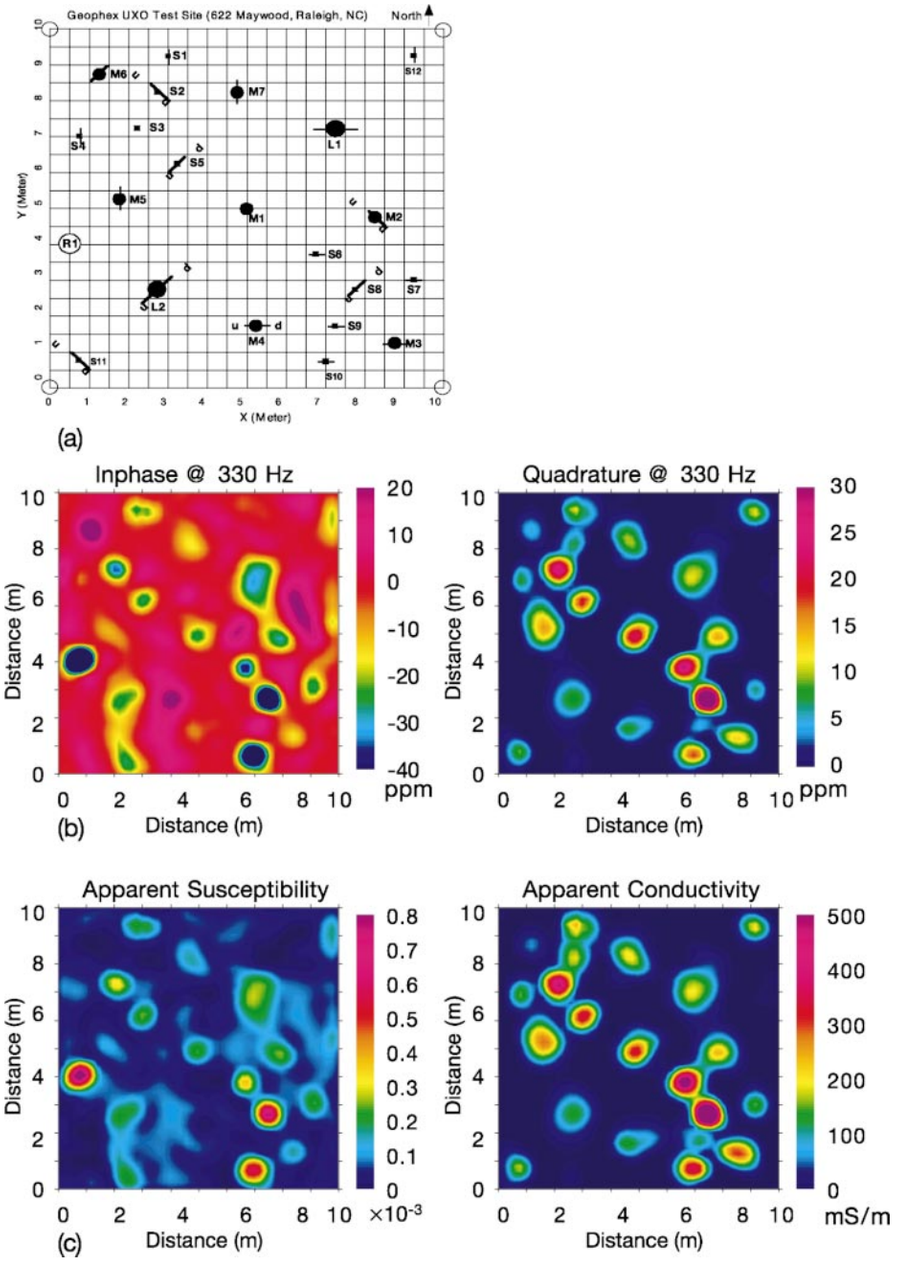

FIG. 10. (a) Geophex UXO test site. (b) In-phase and quadrature maps at 330 Hz. (c) Computed apparent magnetic susceptibility and conductivity maps.

all frequencies because the system is operating in the regime of low induction number where the sounding capability depends on geometry of the source and receiver.

Let's now examine the EM responses σ_a and μ_{ra} for the ferrous metal targets. Figures 5a and 5b illustrate the responses for the ferrous spheres representing ferrous metal targets. The I responses are negative at the lower frequencies and are frequency dependent, indicating that the targets are both magnetic and conductive. The amplitude of the responses depends very much upon the targets' depths. Figures 5c and 5d show κ_a and σ_a, both of which are high for the UXO objects. A comparison of Figure 5 with Figure 4 shows that the values of κ_a and $|I|$ are lower for UXO than for the magnetic rocks in this particular case. This is because the UXD target is small and deep, and the induction effect outweigh the magnetization effect.

We finally examine how the target responses are affected by the background geology. Figures 6a and 6b depict the I and Q responses for both the background geology and the metal objects. They are obtained by adding the two EM responses shown in Figures 4 and 5. The sphere in model I may be detected from the I response alone, based on its frequency dependence. The I response for model II, however, is dominated by the magnetic rock. The sphere is easily detected from the Q response in model I but not in model II because the small anomaly can be easily masked by variations in the soil thickness. Figures 6c and 6d show κ_a and σ_a computed from the I and Q data shown in Figures 6a and 6b based on Figure 2. Ferrous metal targets may not be identified from κ_a amplitude alone because the amplitude is higher for the magnetic rocks than for the targets. However, the targets can be clearly located by σ_a. Comparing the σ_a profile with the Q profile in Figure 6b, the ratio of target-to-host response is significantly enhanced in the σ_a presentation.

EXPERIMENTAL RESULTS

We performed two experiments using the GEM-3 sensor. The first was a series of measurements using different magnetic rocks and metal spheres (ferrous or nonferrous) placed at various distances from the GEM-3. All targets were either buried or on the ground. The results agree well with the numerical modeling discussed above. As an example, we show an experiment using a 12.5-cm-diameter steel shotput and large gneissic (magnetic) rocks placed in red clay soil overlying gneissic bedrock.

First, we collected the I and Q data above the ground outcropping with gneissic rock and background and then converted the data to σ_a and κ_a (Figure 7). The I responses are negative and frequency independent, indicating the geology is magnetic and resistive. The Q responses come from ground conductivity only and not from the magnetic rock. As expected, the gneissic boulder manifests a high κ_a but low σ_a.

Second, we measured the EM response over the shotput in air and converted the data into the σ_a and κ_a as shown in Figure 8. Both the I and Q responses on the shotput are

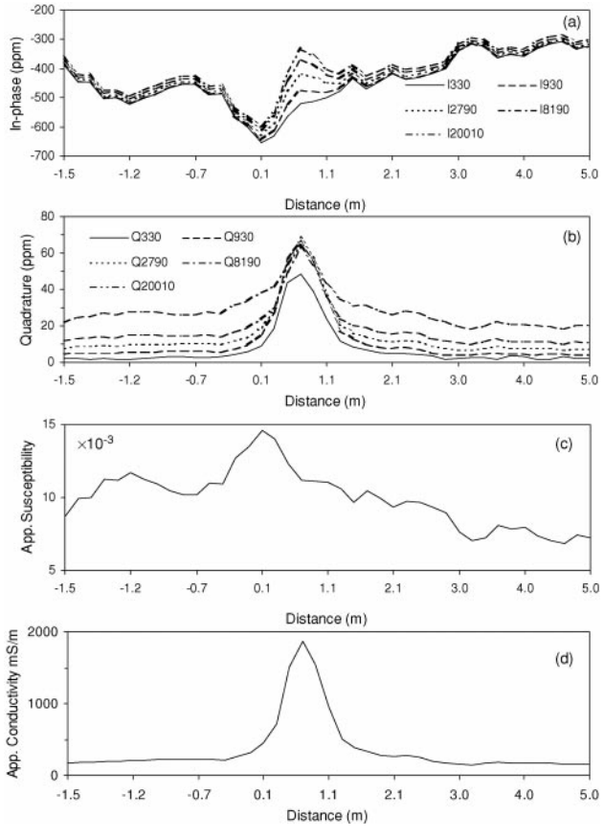

FIG. 11. EM data and their interpretations over a nonferrous metallic object buried in a magnetic geology from a UXO site in Hawaii.

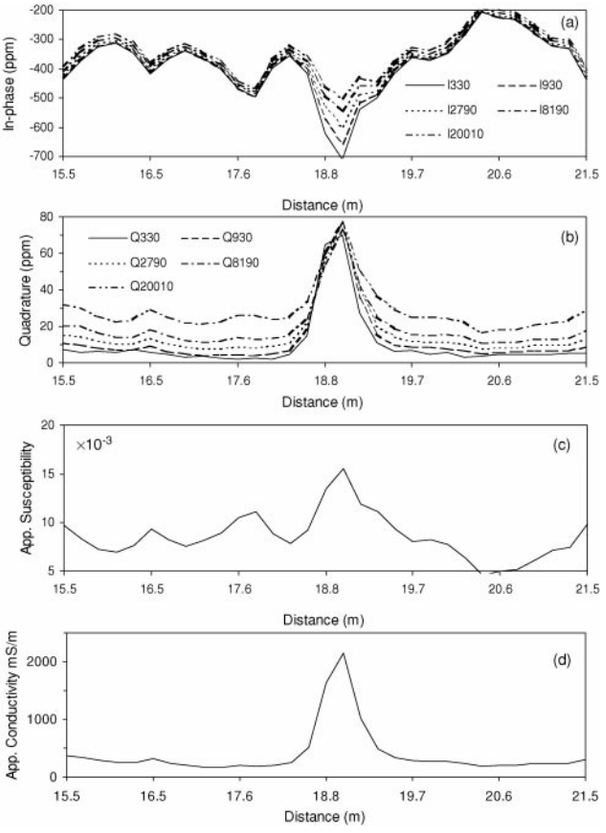

FIG. 12. EM data and their interpretations over a ferrous metallic object buried in a magnetic geology from a UXO site in Hawaii.

large and frequency dependent, indicating the target is both magnetic and conductive. Note that the Q at 330 Hz is almost the same as that at 5370 Hz, and that for 870 Hz is the same as that for 2190 Hz. This is because they are symmetrical with respect to the quadrature peak (see Figure 1b) in this particular case. The shotput obviously has a much higher σ_a than the magnetic rock and geology.

Finally, we buried the shotput next to the diabase boulder. Notice in Figure 9 that the I response from the shotput is distorted by the magnetic rock, while the Q response is not; this is because both contribute to I while only the shotput contributes to Q.

The sum of the I (or Q) data in Figures 7 and 8, shown as circles, is virtually equal to that in Figure 9. The former ignores the effects of inductive coupling and current channeling between the host and metal object, while the latter does not, indicating these effects are negligible.

Our second experiment was performed at a simulated UXO test site, specially designed and constructed by Geophex in Raleigh, North Carolina. The 10×10-m test site shown in Figure 10a contains 21 metal pipes of varying sizes and attitudes and a basketball-size diabase boulder buried in dense, indigenous red clay soil. The locations and descriptions of the objects are shown in Table 2, where z is the depth from the surface to the center of the objects.

Figure 10b shows the GEM-3 I and Q data at 330 Hz collected at 25-cm line intervals (two middle panels) and σ_a and κ_a (two lower panels) derived from the data. The magnetic rock R1 shows a strong anomaly only in the I data, indicating the rock should have high κ_a but low σ_a. All buried objects, including the diabase boulder, clearly show up on the I map, but only metallic objects show up on the Q map. We note that (1) all ferrous metals and the diabase boulder show high κ_a anomalies, (2) nonferrous metals, copper, and aluminum objects cause no κ_a anomaly, and (3) all metal targets produce high σ_a anomalies.

FIELD DATA EXAMPLES

Figure 11 shows the GEM-3 data from a UXO site in Kaho'olawe, Hawaii where highly magnetic bedrock and boulders pose difficulties in detecting buried ordnance because of the magnetic geology. We collected the data at five frequencies (Figures 11a and 11b) and derived the σ_a and κ_a profiles (Figures 11c and 11d). An anomaly at about 0.75 m is observed on the I, Q, and σ_a profiles. From the I data, we note that the target shows obviously frequency-dependent anomalies, while the background geology shows several hundred parts per million below zero that are almost frequency independent. Based on this, we conclude that the anomaly is from a metal object buried in the soil above undulating magnetic bedrock. The high susceptibility at 0.1 m, judging from its low σ_a and Q response, is definitely caused by an isolated magnetic boulder or extruding bedrock. Figure 12 shows another example at 19.1 m, which is interpreted to be a ferrous metal object based on its high κ_a and high σ_a. The two anomalies were confirmed to be ordnance fragments at 12 and 6 inches deep, respectively.

The last field example is from a similar environment in Fort Ord, California. GEM-3 data were obtained at five frequencies: 330, 930, 2790, 8190, and 20 010 Hz. Figure 13 shows the σ_a and κ_a maps derived from the data. A large feature labeled A with high susceptibility but no conductivity is caused by an undulating magnetic basement. Anomalies that manifest both high susceptibility and conductivity are caused by ferrous metal objects such as UXO. Anomaly B is caused by a 1 ft-long and 2-inch-deep ordnance fragment. Likewise, anomalies with high conductivity but no susceptibility are caused by metal objects. Anomaly C is caused by a 1×4-inch nonferrous ordnance fragment at a depth of 2 inches.

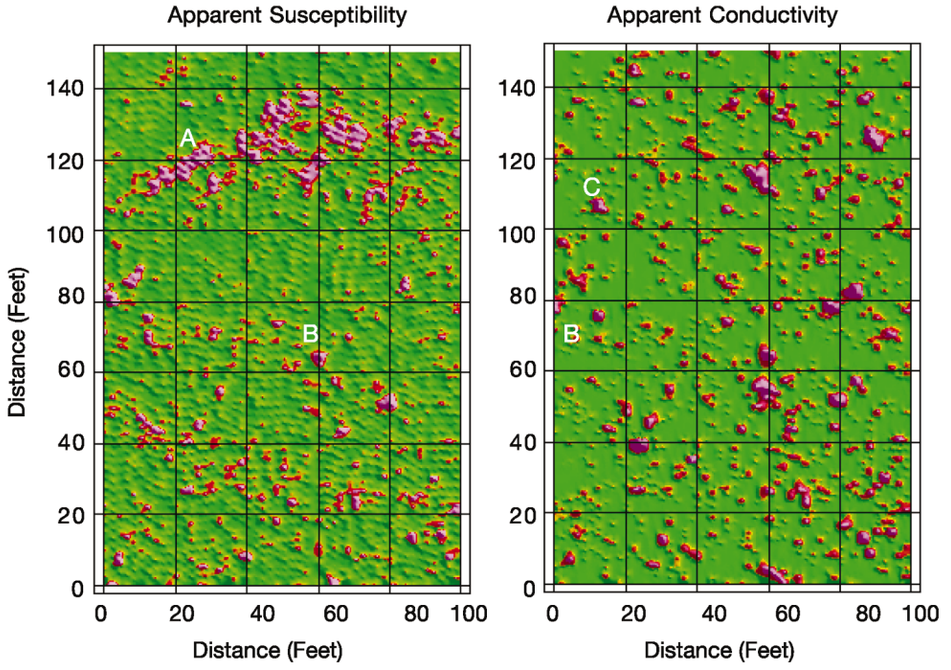

FIG. 13. The apparent susceptibility and conductivity maps converted from GEM-3 data obtained from a UXO site in California where the basement is highly magnetic.

CONCLUSIONS

The broadband EMI sensor can detect small metal targets in magnetic and conductive environments. Outcropping magnetic rocks have much stronger impact on the in-phase data than the magnetic basement and magnetic rocks buried in soil. The former causes a background shift, and the latter causes a very weak anomaly in-phase. While the magnetic geology corrupts significantly the in-phase response, it does not affect the quadrature response or the apparent conductivity derived from the EM data. Therefore, metallic objects like UXO can be detected mainly from the quadrature response or the apparent conductivity.

Algorithms for computing the apparent magnetic permeability and conductivity have been developed for broadband EMI sensors. The lowest frequency is used for apparent magnetic permeability, which, in turn, is used to compute the apparent conductivity from all EM data. Both the apparent conductivity and susceptibility maps help identify ferrous and nonferrous metallic objects against false anomalies caused by magnetic basement and isolated boulders.

ACKNOWLEDGMENTS

This study has been partly funded by the Department of Defense Environmental Security Technology Certification Program (ESTCP) in Arlington, Virginia, and the Naval Research Laboratory in Washington, D.C.

REFERENCES

Fitterman, D. V., and Stewart, M. T., 1986, Transient electromagnetic sounding for groundwater: Geophysics, **51**, 995–1005.

Fraser, D. C., 1978, Resistivity mapping with an airborne multicoil electromagnetic system: Geophysics, **43**, 144–172.

Grant, F. S., and West, G. F., 1965, Interpretation theory in applied geophysics: McGraw-Hill Book Co., Inc.

Huang, H., and Fraser, D. C., 1998, Magnetic permeability and electrical resistivity mapping with a multifrequency airborne EM system: Expl. Geophys., **29**, 249–253.

——— 2000, Airborne resistivity and susceptibility mapping in magnetically polarizable areas: Geophysics, **65**, 502–511.

Huang, H., and Won, I. J., 2000, Conductivity and susceptibility mapping using broadband electromagnetic sensors: J. Envir. Eng. Geophys., **5**, No. 4, 31–41.

Huang, H., Won, I. J., and San Filipo, B., 2003, Detecting buried nonmetal objects using soil magnetic susceptibility measurements, *in* Harmon, R. S., Holloway, J. H., Jr., and Broach, J. T., Eds., Detection and remediation technologies for mines and minelike targets VIII: Proc. SPIE, **5089**, 1181–1188.

Spies, B. R., 1978, Interpretation of transient electromagnetic measurements using the apparent conductivity concept: Bur. Min. Resourc. Austral. Record, 1978/85.

Spies, B. R., and Eggers, D. E., 1986, The use and misuse of apparent resistivity in electromagnetic methods: Geophysics, **51**, 1462–1471.

Wait, J. R., 1951, A conducting sphere in a time-varying magnetic field: Geophysics, **16**, 666–672.

——— 1953, A conducting permeable sphere in the presence of a coil carrying an oscillating current: Can. J. Physics, **31**, 670–678.

——— 1959, Some solutions for electromagnetic problems involving spheroidal, spherical, and cylindrical bodies: J. Res. N.B.S. (Math. and Mathematical Physics), **64B**, 15–32.

——— 1960, On the electromagnetic response of a conducting sphere to a dipole field: Geophysics, **25**, 619–658.

Ward, S. H., and Hohmann, G. W., 1988, Electromagnetic theory for geophysical applications, *in* Nabighian, M. N., Ed., Electromagnetic methods in applied geophysics: Soc. Expl. Geophys., 130–311.

Won, I. J., Keiswetter, D., Fields, G., and Sutton, L., 1996, GEM-2: A new multifrequency electromagnetic sensor: J Environ. Eng. Geophys., **1**, 129–137.

Won, I. J., Keiswetter, D., Hanson, D., Novikova, E., and Hall, T., 1997, GEM-3: A monostatic broadband electromagnetic induction sensor: J. Environ. Eng. Geophys., **2**, 53–64.

Won, I. J., Keiswetter, D., and Novikova, E., 1998, Electromagnetic induction spectroscopy: J. Environ. Eng. Geophys., **3**, 27–40.